

Creating Pores on Graphene Platelets by Low-Temperature KOH Activation for Enhanced Electrochemical Performance

Shuilin Wu, Guanxiong Chen, Na Yeon Kim, Kun Ni, Wencong Zeng, Yuan Zhao, Zhuchen Tao, Hengxing Ji, Zonghoon Lee, and Yanwu Zhu*

KOH activation of microwave exfoliated graphite oxide (MEGO) is investigated in detail at temperatures of 450–550 °C. Out of the activation temperature range conventionally used for the preparation of activated carbons (>600 °C), the reaction between KOH and MEGO platelets at relatively low temperatures allows one to trace the structural transition from quasi-two-dimensional graphene platelets to three-dimensional porous carbon. In addition, it is found that nanometer-sized pores are created in the graphene platelets at the activation temperature of around 450 °C, leading to a carbon that maintains the platelet-like morphology, yet with a specific surface area much higher than MEGO (e.g., increased from 156 to 937 m² g⁻¹). Such a porous yet highly conducting carbon shows a largely enhanced electrochemical activity and thus improved electrochemical performance when being used as electrodes in supercapacitors. A specific capacitance of 265 F g⁻¹ (185 F cm⁻³) is obtained at a current density of 1 A g⁻¹ in 6 m KOH electrolyte, which remains 223 F g⁻¹ (156 F cm⁻³) at the current density of 10 A g⁻¹.

S. Wu, G. Chen, K. Ni, W. Zeng, Dr. Y. Zhao, Z. Tao,
Prof. H. Ji, Prof. Y. Zhu
Key Laboratory of Materials for Energy Conversion
Chinese Academy of Sciences
Department of Materials Science and Engineering
University of Science and Technology of China
96 Jin Zhai Rd, Hefei 230026, China
E-mail: zhuyanwu@ustc.edu.cn

N. Y. Kim, Prof. Z. Lee
School of Materials and Engineering
Ulsan National Institute of Science and Technology
UNIST-gil 50, Ulsan 689-798, Republic of Korea
Prof. H. Ji, Prof. Y. Zhu
iChEM (Collaborative Innovation Center of Chemistry for Energy
Materials)
University of Science and Technology of China
96 Jin Zhai Rd, Hefei 230026, China
Prof. Z. Lee
Center for Multidimensional Carbon Materials
Institute for Basic Science (IBS)
Ulsan 689-798, Republic of Korea

DOI: 10.1002/sml.201503855



1. Introduction

Carbon materials for electrodes in supercapacitors have been extensively investigated in past few decades due to their low cost, high specific surface area (SSA), excellent electrochemical stability, and high electrical conductivity. As a quasi-two-dimensional (quasi-2D) carbon with reasonably high electrical conductivity, chemically reduced graphene oxide with an SSA of 705 m² g⁻¹ was reported to yield a gravimetric capacitance of 99 F g⁻¹ in organic electrolytes and 135 F g⁻¹ in aqueous electrolytes,^[1] which has triggered a large amount of research using graphene-based or graphene-derived materials as electrodes in supercapacitors.^[2–6] The ion-accessible surface area of graphene electrode, which is largely determined by the SSA of graphene material, is the key parameter to high gravimetric capacitance. However, partially due to restacking of graphene platelets in commonly used chemical synthesis, the SSA of many reported graphene materials is much lower than the theoretical SSA of graphene (2630 m² g⁻¹). Thus, many efforts have been made to improve the SSA of graphene-based electrodes or to derive novel

materials with high SSAs from graphene for improved supercapacitor performances. For example, carbon-based nano-spacers, such as carbon nanotubes or fullerenes, have been utilized to intercalate between graphene platelets to prevent the restacking.^[7] In addition, noncarbon nanostructures, such as MgO nanospheres, have also been used as spacers and/or templates in the assembly of graphene oxide (GO) platelets followed by the removal of such spacers in order to generate porous carbons with improved electrochemical performances.^[2] Besides, various processing methods have been developed as well, such as rapid expanding of graphite oxide by heating at 1000 °C,^[8] self-assembly of GO at interface,^[9,10] and chemical activation by alkali compounds.^[11–16]

The chemical activation of carbon has been intensively investigated to prepare porous carbon with a high SSA used as electrode material of supercapacitors for its feasibility and low cost in large-scale production. For example, the mixture of GO and biomass/polymer has been processed with KOH, yielding a carbon with an SSA of 3523 m² g⁻¹ and a gravimetric capacitance of 231 F g⁻¹.^[11] KOH activation has also been applied to carbon fibers and multiwalled carbon nanotubes (MWCNTs) for improving their electrochemical performances as electrodes in supercapacitors.^[17,18] When KOH activation was utilized to process graphene materials, e.g., microwave exfoliated graphite oxide (MEGO), a three-dimensional (3D) porous carbon named aMEGO with a SSA of up to 3100 m² g⁻¹ has been obtained, yielding a gravimetric capacitance of 166 F g⁻¹ in organic electrolyte.^[12] Zhang et al. reported a highly porous (SSA of 2400 m² g⁻¹) yet freestanding and conductive graphene paper by KOH activation, which exhibits an outstanding rate capability.^[6] The improved electrochemical performance of KOH-activated carbons is ascribed to the high SSA contributed by nanopores. However, the large pore volume in such carbons, e.g., aMEGO reported previously, has led to a sacrifice in density (the density of as-prepared aMEGO electrodes is about 0.35 g cm⁻³),^[12] thus resulting in a relatively low volumetric performance and hampering their application in practical supercapacitor devices.^[19,20] On the other hand, a proper stacking of graphene platelets has shown efficiency to improve the density of electrodes for superior volumetric performance of supercapacitors.^[21] Thus, the SSA and density is trade-off in KOH-activated carbon materials. Investigation of KOH activation under relatively mild conditions may benefit to the balance between porosity and density, possibly leading to a carbon with performance toward practical energy storage devices.

In general, KOH activation for the preparation of activated carbons has been classified into three stages based on the range of reaction temperatures:

- (i) Carbon etching by redox reaction $2C+6KOH\rightarrow 2K+2K_2CO_3+3H_2$ at temperatures of above 400 °C;
- (ii) Nanopores created by CO₂ (g) and H₂O (g) that are produced by K₂CO₃ decomposition at temperatures of above 700 °C;
- (iii) Carbon lattice expansion by K vapor intercalation at temperatures of above 800 °C, which is irreversible after the removal of K by washing with solvents.

It has been widely accepted that KOH activation is less effective at temperatures of lower than 600 °C.^[13–15] In addition, KOH activation of well-sp²-hybridized carbons, e.g., MWCNTs or graphene platelets, could be different due to the probably different reaction path between KOH and sp²-hybridized carbons. Murali et al. investigated the effects of KOH/C ratio and activation temperature on SSA and electrochemical capacitance of aMEGO at temperatures of above 600 °C, and the results showed that both SSA and specific capacitance are maximized for the aMEGO obtained at around 800 °C.^[16] Raymundo-Piñero et al. investigated the activation mechanism of MWCNTs with KOH and NaOH.^[13] The results showed that the reaction between MWCNTs and KOH begins at around 400 °C, forming K₂CO₃; KOH is fully transformed to K₂CO₃ at 600 °C, followed by a decomposition of K₂CO₃ to K₂O and CO₂ at 700 °C. The activation is eventually ended by intercalation of K between graphitic walls of MWCNTs at temperatures of above 800 °C. Interestingly, no significant restructuring has been observed among the walls of MWCNTs or MWCNTs.

Therefore, the activation process of graphene materials may largely determine the microstructure of carbons obtained, such as the defects, edges, and dopants, which are important features influencing the electrochemical performance. For example, Kim et al. showed that the edges of platelets and herringbone carbon fibers can contribute three to five times more than the basal plane surface of tubular carbon fibers to capacity.^[22] The heteroatom doping in graphene could dramatically enhance the electrochemical performance via changing the electronic properties of electrode materials and providing pseudocapacitance.^[23] Further, Ambrosi et al. revealed that doping-induced structure defects are the dominant factors influencing capacitance which is weakly related to the doping type and level.^[24] Zhang et al. suggested that the edges of graphene may contribute to more surface areas, leading to an SSA of even exceeding the theoretical SSA of graphene.^[11] Besides, the planar pores in graphene may provide more diffusion channels for ions, which may increase the rate capability.^[25] Thus, it is desirable to study the KOH activation of graphene to understand the evolution of the macrostructure (e.g., SSA) and the microstructure (e.g., defects, edges, pore morphology, and size) with activation parameters, thereby achieving the balance between the gravimetric and the volumetric capacitance for the practical application of graphene in supercapacitors.

Inspired by the suggested KOH activation mechanism, the activation under relatively mild conditions may benefit to the balance between porosity and density. In this work, the KOH activation of MEGO is carefully controlled in a temperature range of 450–550 °C. It is found that, instead of reconstructing graphene to 3D carbon, the KOH etching at such temperatures creates more pores in graphene platelets, resulting in a carbon with quasi-2D morphology yet with a much higher SSA than MEGO. Electrochemical measurements indicate that in-plane pores introduced by KOH etching largely contribute to the capacitance, leading to a specific capacitance of 265 F g⁻¹ at the current load of 1 A g⁻¹, which retains 223 F g⁻¹ at 10 A g⁻¹.

2. Results and Discussion

2.1. Morphology and Structure

Typical transmission electron microscope (TEM) images of MEGO and low temperature activated graphene (LTAG) samples were shown in **Figure 1** and Figure S1 (Supporting Information), from which we can clearly see that MEGO consists of crumples and stacking of reduced graphene oxide platelets, as reported before.^[27] By contrast, LTAG-500-10 shows a much smoother surface with much less crumples. For the samples of LTAG-450 obtained from activation at the temperature of 450 °C, more lamellar structures are maintained, as observed from TEM images of LTAG-450-3 (Figure S1a,b, Supporting Information) and LTAG-450-10 (Figure S1g,h, Supporting Information).

Comparatively, LTAG-500 samples are still lamellar structure with less crumples. As the activation temperature further increases, e.g., to 550 °C, an evolution from the lamellar structure to a 3D porous structure is observed, as shown in Figure S1 (Supporting Information). With increase in the activation temperature or the activation duration, the density of crumples shows a consistent decrease for LTAG samples. For the same activation temperature, the density of pores increases with the duration of activation process. Besides, the scanning electron microscope (SEM) images of MEGO and all LTAG samples were also shown in Figure S3 (Supporting Information). From the SEM images, crumpled thin flakes can be observed in MEGO and LTAG samples except for LTAG-550-10, indicating that the flake-like morphology has been well maintained under relatively mild activation conditions. By contrast, LTAG-550-10 shows a chunk-like morphology (Figure S3m,n, Supporting Information), which is more similar with aMEGO samples reported previously.^[12] The internal structure of LTAG-550-10 is highly porous as observed from TEM images (Figure S1i,j, Supporting Information), indicating that a restructuring has occurred upon activation of MEGO at 550 °C for 10 h.

In order to characterize the pore structure in detail, high resolution transmission electron microscope (HR-TEM) was conducted at 80 kV with a monochromator and typical images of LTAG-500-10 are shown in **Figure 2**. From Figure 2, we can clearly see holes with diameters of 3–4 nm or ≈8 nm distributed in thin platelets, which are consistent with pore size distribution obtained from the nitrogen adsorption/desorption isotherms as shown below (Figure 4c). With higher magnification, Figure 2b shows both carbon planes and circular strings observed in very thin areas in LTAG-500-10. An area with uniform contrast has been zoomed in and the

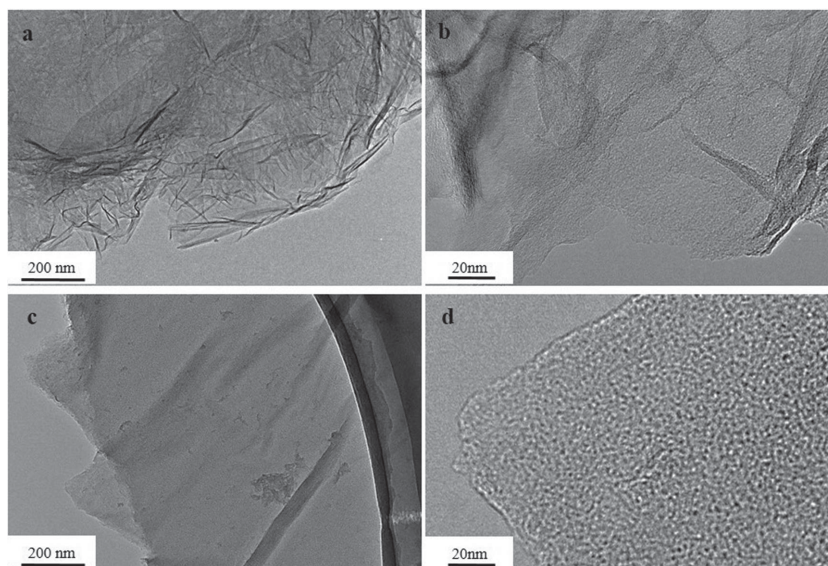


Figure 1. a,b) TEM of MEGO. c,d) LTAG-500-10 at various magnifications.

HR-TEM image is shown in the upper inset of Figure 2b, from which a multi-crystal feature can be observed. With the assistance of fast Fourier transformation analysis (lower inset of Figure 2b), the area corresponds to a region with locally distributed hexagons yet a short-range ordering; the lattice constant is estimated to be 2.02 Å, close to 2.13 Å in graphene.^[27] Thus, the basic plane of LTAG-500-10 is still close to that of MEGO, considering the existence of O and H residues. The strings may be related to those graphene layers parallel to the electron beam. The relatively random distribution and small sizes of such layers could be explained by the etching caused in KOH activation process. Through etching by KOH, graphene sheets became holy or broken into small pieces. The random distribution of graphene sheets was inherited from MEGO, which was developed from the microwave exfoliated process.^[26] Compared to highly curved strings or stripes observed in aMEGO that were activated at 800 °C,^[12] the strips in LTAG-500-10 are relatively straight, consistent with the smoother morphology of LTAG than that of MEGO or aMEGO. The interlayer distance of such stripes is 3.42 Å, slightly larger than that of 3.35 Å in graphite, partially due to the residual oxygen group. Tilting experiments were conducted in HR-TEM in order to further

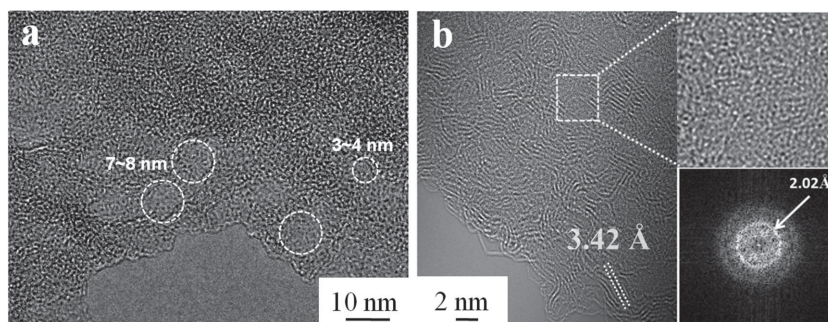


Figure 2. a) Morphology of LTAG-500-10 with mesopores labeled with dashed circles. b) HR-TEM images of LTAG-500-10. Top right inset shows the zoomed image of white dashed region and bottom right inset shows the Fast Fourier transformation of the zoomed region.

investigate the strips, and the images of the same region at different tilting angles were shown in Figure S2 (Supporting Information). We can see that as the tilting angle changes, the strips marked in the green circle disappear, while other strips emerge in the region where no strips were observed previously. The result suggests that there are randomly distributed, thin graphene nanoplatelets in LTAG-500-10, although the typical morphology is smooth flakes.

Powder X-ray diffraction (XRD) of MEGO and LTAG samples is shown in Figure 3a and Figure S4 (Supporting Information). The XRD spectrum of MEGO (Figure 3a) shows a peak at 23.2° , which can be attributed to the (002) interlayer distance as the residual oxygen groups and/or crumples may make the distance larger than that in graphite. The LTAGs that were activated at temperatures of 450, 500 and 550°C have (002) diffraction peaks located at 25.7° , 25.7° , and 24.5° , respectively, indicating a smaller layer distance of graphene sheets after activation. Such an upper shift of (002) diffraction peak of LTAG samples is related to the further removal of residual oxygen groups (Figure 3d and Figure S5, and Table S2, Supporting Information) and reduced crumples of graphene sheets (Figure 1; Figures S1 and S3, Supporting Information) in LTAG samples after the activation process. However, when the activation was carried out at 550°C , e.g., in the case of LTAG-550-3, the (002) peak intensity becomes lower and the position shifts to a lower angle, e.g., 24.5° , indicating less ordering of graphitic layers and a larger interlayer distance. We suggest that the activation process removes oxygen groups and reduces wrinkles on MEGO, thus, the LTAGs obtained at different temperatures have a smaller interlayer distance than that of MEGO (Figure 1; Figures S1 and S3 and Table S2, Supporting Information), yet

reconstruction among carbon atoms occurs with increasing the activation temperature, leading to an expanded interlayer distance.^[6,11,12]

The numbers of the spins of graphene is a measure of the concentration of the dangling bonds.^[12] Electron paramagnetic resonance (EPR) was carried out at 2 K to trace the change in spins caused by activation processing. Figure 3b shows EPR curves of LTAG samples activated for 3 h and the curves from other samples are shown in Figure S6 (Supporting Information). Since the signal of carbon dangling bonds is weak at room temperature, the tests were conducted at 2 K to enhance the spin signal and inhibit the noise from environment. All values in the curves have been normalized to the weight of each sample. By comparing the data from LTAG samples with that from 2,2-diphenyl-1-picrylhydrazyl (DPPH), the number of spins is estimated to be 2.5×10^{23} , 4.66×10^{23} , 9.48×10^{23} , 1.9×10^{23} , 4.68×10^{22} , or 3.99×10^{22} spins g^{-1} for LTAG-450-3, LTAG-450-10, LTAG-500-3, LTAG-500-10, LTAG-550-3, or LTAG-550-10, respectively. As summarized in Figure 3c, the EPR intensity increases first with the activation temperature for the samples treated for 3 h, then drops to a low concentration of 4.68×10^{22} spins g^{-1} (black curve in Figure 3c), yet the EPR intensity decreases monotonically with the temperature with 10-h activation. This result further supports our assumption based on TEM and XRD studies that the activation process begins with the etching of graphene matrix via redox reaction between C and KOH and the reconstruction of graphene fragments needs a higher temperature. When heated at 450°C , the reaction between C and KOH dominates in the activation process which leaves defects and planar pores. At 500°C , the rate of the reaction between C and KOH is higher due to the higher

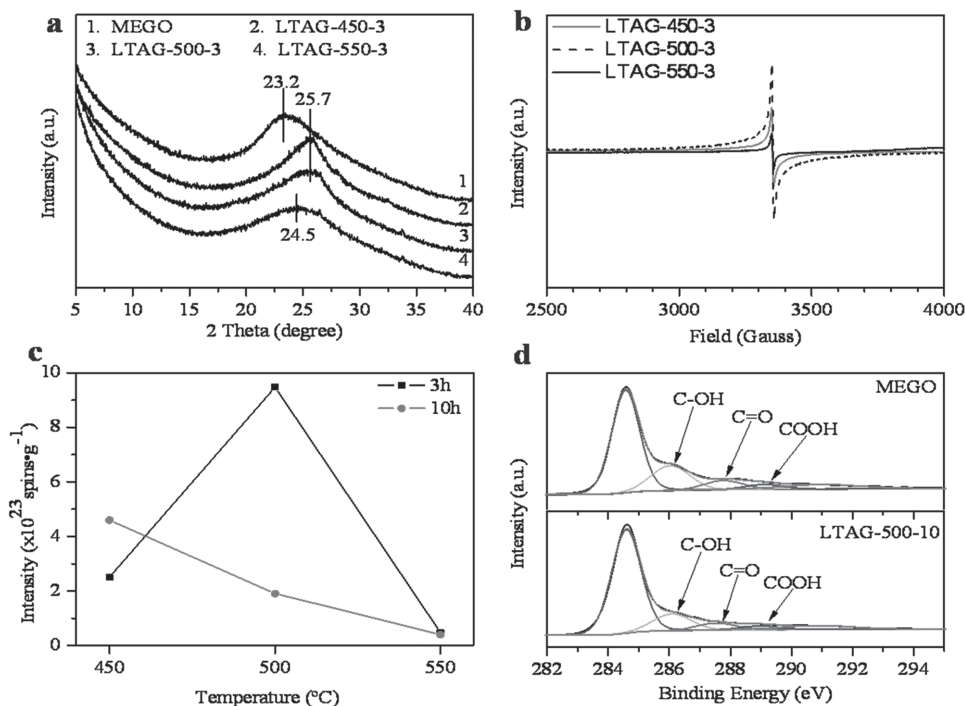


Figure 3. a) Powder X-ray Diffraction of MEGO and LTAG samples. b) Electron Paramagnetic Resonance of LTAGs. The data were measured at 2 K to enhance the signal and inhibit the environment noise. As-measured values have been normalized to the mass of each sample. c) The normalized specific spins of LTAGs when DPPH was used as a reference. d) XPS C1s spectra of MEGO and LTAG-500-10.

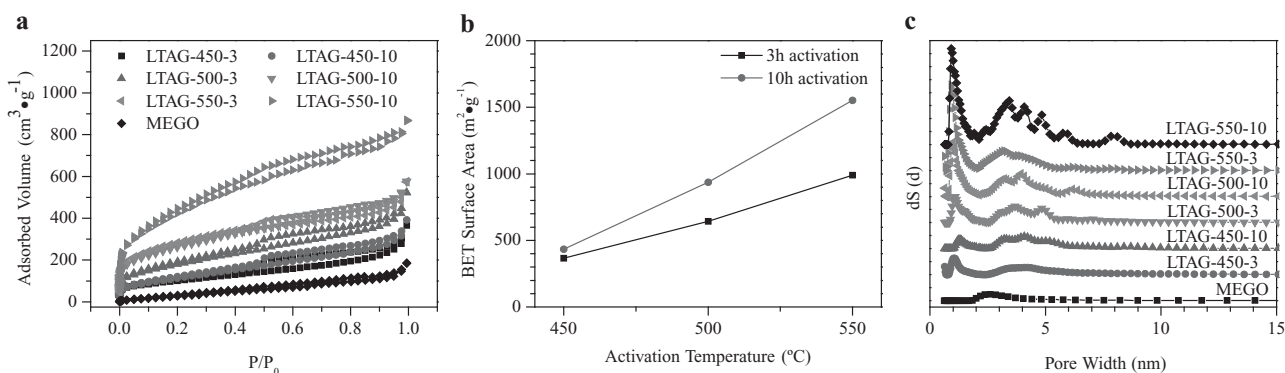


Figure 4. a) Nitrogen adsorption/desorption isotherms of MEGO and LTAG samples. b) BET SSA of LTAG samples at different activation conditions; c) Pore width analysis with QSDFT method.

temperature, yet the reconstruction among carbon fragments occurs slightly. So the EPR intensity of LTAG-500-3 is larger than that of LTAG-450-3. When extending the activation process, the reaction between C and KOH reaches saturation or equilibrium as the concentration of defects or dangling bonds increases; meanwhile, the rate of reconstruction enhances. Therefore, the LTAG-500-10 has a lower spin than that of LTAG-500-3. At 550 °C, the reconstruction dominates the activation process, thus the LTAG-550-3 and LTAG-550-10 have a similar and the lowest EPR intensity compared to that of the other samples.

Nitrogen adsorption/desorption has been used to investigate the change in SSA of MEGO upon KOH activation. Isotherms of nitrogen adsorption/desorption at 77 K are shown in **Figure 4a**. All isotherms of LTAG samples demonstrate a feature of H4 type hysteresis loops, according to the International Union of Pure and Applied Chemistry (IUPAC) classification,^[28] which appear to be associated with narrow slit-like pores. In contrast, the isotherm of MEGO shows nearly indistinguishable hysteresis, partially due to its low pore volume. At low pressures, LTAG samples demonstrate obviously enhanced filling of micropores. SSA values calculated by Brunauer–Emmett–Teller (BET) method are summarized in **Figure 4b**.^[29] The BET SSA of MEGO is 156 m² g⁻¹, which is lower than 463 m² g⁻¹ previously reported, possibly due to the relatively low exfoliation/expansion degree of MEGO used in this work.^[26] Both pore volume of micropores and BET SSA increase with the temperature of the activation process or the activation duration. A quenched solid density function theory (QSDFT) has been used to

obtain the pore size distribution from isotherms as this model takes the surface roughness of pores into account.^[30] From the pore size distribution shown in **Figure 4c**, MEGO has almost no micropores (pore width of 0–2 nm) but a wide distribution of mesopores, probably originated from the disordered stacking of graphene platelets. With slight activation, the pore size distribution of LTAG-450-3 is similar to that of MEGO except emerging of micropores, suggesting that creating micropores starts at the initial stage of activation. For higher activation temperatures, micropores are further developed and the size distribution of mesopores is narrowed down to around 4 nm, as observed from the curves of LTAG-500-3 and LTAG-550-3. Extending the activation process at a certain temperature broadens the pore size distribution, e.g., in the case of LTAG-550-10, which may be attributed to the restructuring of the platelets in which the interconnected pores start to form.

As can be seen above, the activation at relatively low temperatures has allowed us to trace the structural evolution from quasi-2D MEGO to 3D aMEGO. **Figure 5** schematically describes the transition of MEGO when being processed in KOH from 450 to 550 °C. At the initial stage of activation, KOH etches the graphene platelets and creates more defects and pores via redox reactions. At the same time, the surface tension of melted KOH pulls out the crumples and the platelets become flatter. Further, some graphene platelets break into small pieces and the random distribution of pieces or stripes results in more mesopores with increase in the degree of the activation. At higher temperature or after longer treatment, e.g., at 550 °C for 10 h, more broken

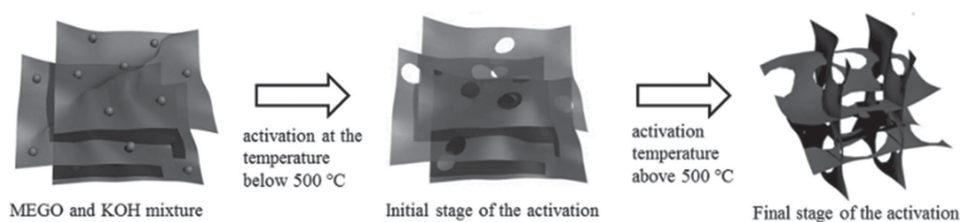


Figure 5. Schematic describing the transition of quasi-2D MEGO to 3D porous structure. The MEGO and KOH mixture (left), the initial stage of the activation, graphene plates were etched or cut into small pieces via redox reaction with KOH when the activation temperature was below 500 °C (medium), the reconstruction among fragments into 3D porous structures when the activation temperature was above 500 °C (right).

carbon species and thus more dangling bonds trigger the restructuring, leading to the formation of 3D carbon architecture in a MEGO.

2.2. Chemical Composition

The chemical environment of LTAG samples was investigated with X-ray photoelectron spectroscopy (XPS) and Fourier transform infrared spectroscopy (FTIR). The XPS C1s spectra of MEGO and LTAG samples are shown in Figure 3d and Figure S5 (Supporting Information), in which peaks at 284.6, 286.0, 287.4, and 289.0 eV are assigned to C=C sp² bonding, C–OH, C=O and COOH groups, respectively.^[31] As can be seen from the peak areas listed in Table S1 (Supporting Information), C–OH in MEGO has been further removed in the KOH processing at 500 °C for 10 h. With KOH activation, the area of peak assigned to C=O slightly decreases, while the peak attributed to COOH remains unchanged or appears to increase slightly. Calculated from XPS survey spectrum, the contents of carbon and oxygen are listed in Table S2 (Supporting Information). The oxygen contents of LTAG samples are lower than that of MEGO, indicating the KOH activation removes oxygen, especially that in C–OH and C=O groups. FTIR and Raman spectra of LTAGs and MEGO are shown in Figures S7 and S8 (Supporting Information), respectively. From both characterizations, LTAG samples demonstrate features similar to MEGO,^[27] suggesting that the change in functional groups or defects (pores, edges and non-hexagonal rings) is not so significant with the activation at such low temperatures, in terms of response from FTIR and Raman spectroscopy.

2.3. Electrochemical Performance

The electrochemical performance of LTAG-500-10 was investigated by cyclic voltammetry, galvanostatic charge–discharge, and electrochemical impedance spectroscopy (EIS) in 6 M KOH aqueous electrolyte. For a better comparison, as-purchased MEGO was annealed at 500 °C for 10 h (leading to a sample named as MEGO-500-10-anneal) and measured as a reference. **Figure 6** illustrates cyclic voltammograms (CVs) at different scan rates, charge–discharge curves at different current loadings, Nyquist plots obtained from EIS, which were all tested in a symmetrical two-electrode cell. As we can see in Figure 6a, the shape of CV curves for LTAG-500-10 is quasi-rectangular with humps, indicating that the capacitance of LTAG-500-10 is related to both electrical double-layer capacitance and pseudocapacitance. By comparing the CV areas in Figures 6a and 6b, we can see that LTAG-500-10 has a higher specific capacitance than MEGO-500-10-anneal or as-purchased MEGO (shown in Figure S10, Supporting Information). In addition, the redox peaks of LTAG-500-10 at high potentials are weaker than those of MEGO-500-10-anneal or MEGO in the same potential ranges. XPS studies have shown that MEGO has the highest content of oxygen among all the samples studied, while LTAG-500-10 and MEGO-500-anneal consist of similar oxygen contents (Table S2, Supporting Information). Thus, the residual oxygen

groups in LTAG-500-10 may not be dominating to the capacitance. Instead, the enhanced capacitance in LTAG-500-10 may result from the planar pores induced by the activation process. The CV curves of LTAG-500-3 and LTAG-550-3 samples are also shown in Figure S9c,d (Supporting Information) as a reference. Comparing the CV areas of these samples (LTAG-500-3, LTAG-500-10, and LTAG-550-3), LTAG-500-10 shows the best specific capacitance, LTAG-550-3 shows the worst. Considering that the SSA of LTAG-500-10 is larger than that of LTAG-500-3, but similar to that of LTAG-550-3, the high specific capacitance of LTAG-500-10 may indicate the planar pores are more efficient in charge storage.

The galvanostatic charge–discharge curves of LTAG-500-10 and MEGO-500-10-anneal are shown in Figure 6c,d, and those of MEGO shown in Figure S10b (Supporting Information). They all have linear curves, which indicate the existence of fast redox reactions during the charge–discharge process. The specific capacitances calculated from the results of charge and discharge curves at different current loads are shown in Figure 6e. LTAG-500-10 has a specific capacitance of 265 F g⁻¹ at 1 A g⁻¹ and 223 F g⁻¹ at 10 A g⁻¹, while the capacitance of MEGO-500-10-anneal is 80 F g⁻¹ at 1 A g⁻¹ and 52 F g⁻¹ at 10 A g⁻¹. The excellent rate capability of LTAG-500-10 could be due to the effective ion diffusion channels provided by planar pores.^[25] The specific volume capacitance of LTAG-500-10 is 185 F cm⁻³ at 1 A g⁻¹, calculated from the specific mass capacitance and the density, which is about 0.7 g cm⁻³ for the electrode membranes. By comparing the Nyquist plots of LTAG-500-10 and MEGO-500-10-anneal shown in Figure 6f, also those of LTAG-500-3 and LTAG-550-3 shown in Figure S9 (Supporting Information), LTAG-500-10 shows the shortest diameter of the semi-circle at high frequencies, indicating the lowest charge transfer resistance, that is, the ion can transfer/diffuse easily among the porous structures. This, in addition, fortifies the assumption that planar pores provide an efficient charge transfer channel.

To investigate the effect of structure evolution on the cycling stability, the cycling performance of samples obtained from activation performed at various temperatures has been measured at the same constant current of 15 A g⁻¹, as shown in Figure S11 (Supporting Information). As we can see, LTAG-500-10 shows a higher retention than LTAG-450-10 after 5000 cycles of testing. Obtained from activation at a higher temperature such as 550 °C, LTAG-550-3 demonstrates only a slight degradation before 2000 cycles and a linear trend after that. Considering that higher activation temperatures and/or longer activation durations benefit the restructuring of lamellae graphene platelets to 3D structure as discussed above, the different stability among the samples could be related to the morphological/structural changes under such mild activation conditions. It is worth noting that the stability of electrodes in supercapacitors could be influenced by many factors, especially when pseudocapacitance is involved. Even when the factors from active materials are solely considered, e.g., LTAG samples discussed here, oxygen containing groups, in-plane holes, edges and so on, could contribute to the instability in cycling more than a possible restacking of platelets that occurred in repeated charging and discharging.

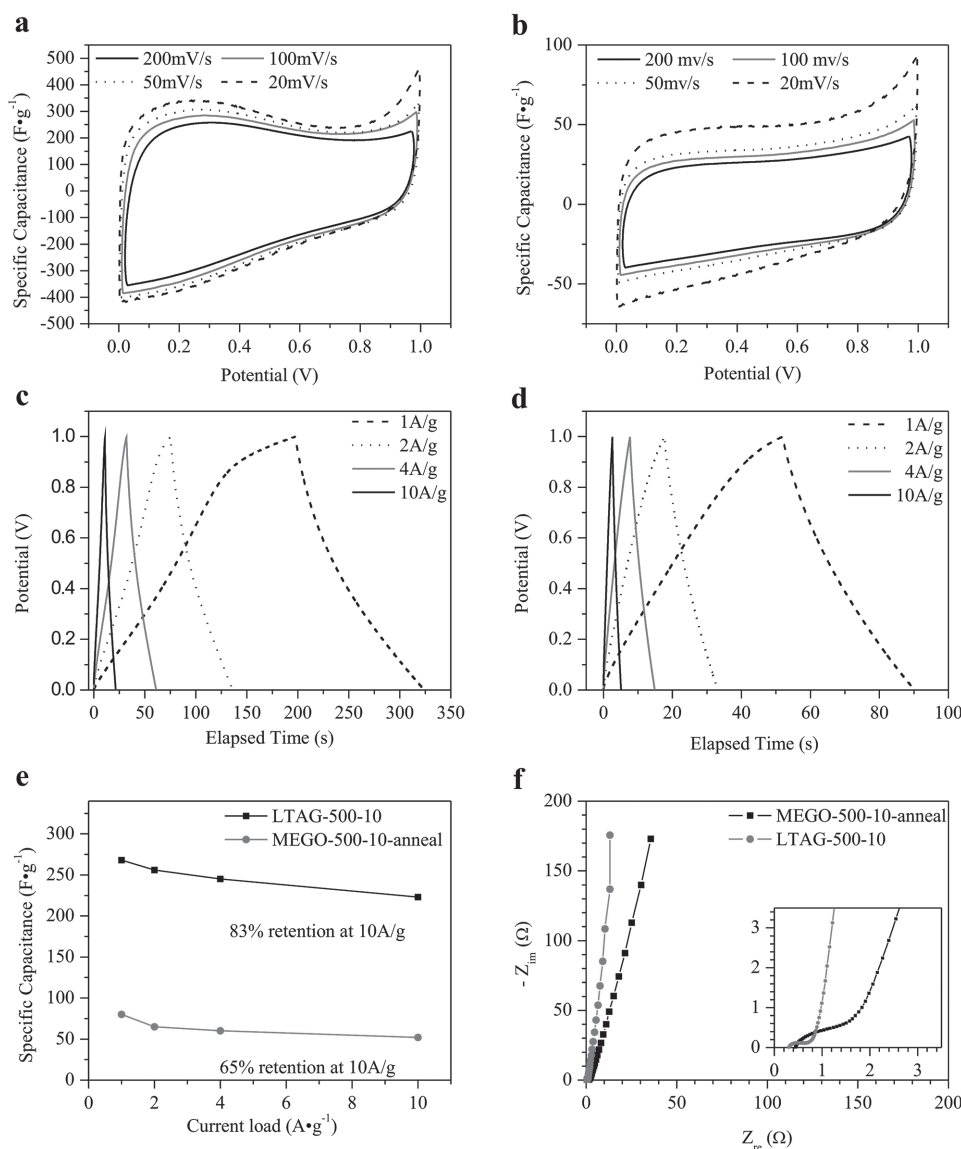


Figure 6. Cyclic voltammetry curves of a) LTAG-500-10 and b) MEGO annealed at 500 °C for 10 h at different scan rates. Galvanostatic charge–discharge curves of c) LTAG-500-10 and d) MEGO annealed at 500 °C for 10 h at different current loads. e) Rate capability of LTAG-500-10, MEGO annealed at 500 °C for 10 h. f) Nyquist curves of LTAG-500-10 and MEGO annealed at 500 °C for 10 h.

3. Conclusions

In conclusion, the mechanism of MEGO activation by KOH has been investigated by treating MEGO in KOH at relatively low temperatures. Two stages, namely etching and restructuring are observed, corresponding to the reactions between graphene plates and KOH at temperatures below 500 °C and interconnection of carbon species at temperatures above 500 °C, respectively. Before MEGO is transformed from the flake-like structure to the 3D porous carbon, micro- and mesopores in graphene platelets have been created via precisely controlling the activation process. Through the etching process by the redox reaction between C and KOH, a porous graphene with a SSA of 1532 m² g⁻¹ can be obtained, showing that the activation of carbon is still efficient at mild condition, yet the density remained. When the porous yet platelet-like carbon is tested as electrodes for supercapacitors, the specific

capacitance and rate capability have been largely enhanced, indicating the tailoring pores in graphene platelets stacking could be an efficient strategy to improve the electrochemical storage in graphene-based materials.

4. Experimental Section

LTAG: Typically 200 mg MEGO (purchased from The Sixth Element Co. Ltd.) was mixed with 12.0 g potassium hydroxide (analysis grade, purchased from Sinopharm Chemical Reagent Co. Ltd.) and loaded into a nickel boat, then heated in Ar with a flow rate of 100 sccm. Three temperatures (400, 450, or 500 °C) and two durations (3 or 10 h) were used to perform the activations. After activations, samples were sequentially washed by 1 M hydrochloric acid (HCl), deionized water, and ethanol. Washed samples were further dried at 60 °C in ambient conditions for 10 h.

Samples obtained are thus named by the activation temperature and duration, e.g., LTAG-500-10, indicating that the sample was obtained from the activation at 500 °C for 10 h.

Characterizations: Structure of LTAG was investigated by using XRD with Cu-K α radiation ($\lambda = 1.5418 \text{ \AA}$, Rigaku SmartLab). Morphology of LTAG was investigated using field-emission scanning electron microscopy (FE-SEM, JEOL-6700F, 5 kV), transmission electron microscopy (FE-TEM, JEOL-2100F, 200 kV), and high-resolution transmission electron microscopy with an electron monochromator (HR-TEM, FEI-Titan G2 60–300, 80 kV). To prepare TEM samples, LTAG powder was dispersed in ethanol and sonicated for 30 min. X-ray photoelectron spectroscopy (XPS) was carried out on Thermo ESCALAB 250 with an Al K α radiation. Nitrogen adsorption/desorption was performed at 77.4 K on Quantachrome Autosorb iQ to obtain the SSA and pore size distribution. Prior to adsorption/desorption measurements, all samples were degassed at 200 °C for 12 h under vacuum. EPR was performed at 2 K with a liquid Helium accessory on Bruker ELEXSYS II system, under a microwave irradiation power of 100 μ W. The magnification factor was 10 000 for LTAG samples and 200 for 2,2-diphenyl-1-picrylhydrazyl (DPPH). DPPH (Alfa Aesar, 95% purity) was diluted with CaCO $_3$ (analysis grade, Sinopharm Chemical Reagent Co. Ltd.) as a reference.

Electrochemical Measurements: A two-electrode-cell configuration was used to evaluate the supercapacitor performance of LTAG electrodes.^[32] To prepare the electrodes, 5 wt% polytetrafluoroethylene (PTFE; 60 wt% dispersion in water as purchased from Sigma) was added to LTAG powders and mixed using a mortar and pestle. The mixture was then rolled into a membrane and punched into 6-mm-diameter electrodes with about 40 μ m thick and 1.0 mg weight for each. Before electrochemical testing, the electrodes were immersed in 6 M KOH for 3 d. Porous polypropylene (Celgard 3501) was used as separator and platinum foils used as current collectors. All electrochemical measurements were performed on PARSTAT 4000 (Princeton Applied Research, AMETEK).

Gravimetric capacitance was calculated from galvanostatic discharge curves by using formula

$$C = \frac{4I}{m dV/dt}$$

Where I is the constant current for charge/discharge, m the total mass for two identical electrodes, and dV/dt the slope of discharge curves in the range of the maximal voltage V_{\max} to V_{\min} (usually 0 V).^[32]

Supporting Information

Supporting Information is available from the Wiley Online Library or from the author.

Acknowledgements

The authors appreciate the financial support from the China Government 1000 Plan Talent Program, the China MOE NCET Program, the Natural Science Foundation of China (51322204), the Fundamental

Research Funds for the Central Universities (WK2060140014 and WK2060140017) and the External Cooperation Program of BIC, and the Chinese Academy of Sciences (211134KYSB20130017). This work was also supported by the National Research Foundation of Korea (NRF) grant funded by the Korea government (MSIP) (Grant No. 2015R1A2A2A01006992). This work was also supported by IBS-R019-D1. The authors also thank the Steady High Magnetic Field Facility for the EPR characterizations, the High Magnetic Field Laboratory, CAS.

- [1] M. D. Stoller, S. J. Park, Y. W. Zhu, J. H. An, R. S. Ruoff, *Nano Lett.* **2008**, *8*, 3498.
- [2] J. Yan, Q. Wang, T. Wei, L. L. Jiang, M. L. Zhang, X. Y. Jing, Z. J. Fan, *ACS Nano* **2014**, *8*, 4720.
- [3] Z. J. Fan, Q. K. Zhao, T. Y. Li, J. Yan, Y. M. Ren, J. Feng, T. Wei, *Carbon* **2012**, *50*, 1699.
- [4] Z. Q. Niu, J. Chen, H. H. Hng, J. Ma, X. D. Chen, *Adv. Mater.* **2012**, *24*, 4144.
- [5] T. Kim, G. Jung, S. Yoo, K. S. Suh, R. S. Ruoff, *ACS Nano* **2013**, *7*, 6899.
- [6] L. L. Zhang, X. Zhao, M. D. Stoller, Y. W. Zhu, H. X. Ji, S. Murali, Y. P. Wu, S. Perales, B. Clevenger, R. S. Ruoff, *Nano Lett.* **2012**, *12*, 1806.
- [7] D. S. Yu, L. M. Dai, *J. Phys. Chem. Lett.* **2010**, *1*, 467.
- [8] M. J. McAllister, J. L. Li, D. H. Adamson, H. C. Schniepp, A. A. Abdala, J. Liu, M. H. Alonso, D. L. Milius, R. Car, R. K. Prud'homme, I. A. Aksay, *Chem. Mater.* **2007**, *19*, 4396.
- [9] F. Kim, L. J. Cote, J. X. Huang, *Adv. Mater.* **2010**, *22*, 1954.
- [10] C. M. Chen, Q. H. Yang, Y. G. Yang, W. Lv, Y. F. Wen, P. X. Hou, M. Z. Wang, H. M. Cheng, *Adv. Mater.* **2009**, *21*, 3541.
- [11] L. Zhang, X. Yang, G. K. Long, Y. P. Wu, T. F. Zhang, K. Leng, Y. Huang, Y. F. Ma, A. Yu, Y. S. Chen, *Sci. Rep.* **2013**, *3*, 1408.
- [12] Y. W. Zhu, S. Murali, M. D. Stoller, K. J. Ganesh, W. Cai, P. J. Ferreira, A. Pirkle, R. M. Wallace, K. A. Cychosz, M. Thommes, D. Su, E. A. Stach, R. S. Ruoff, *Science* **2011**, *332*, 1537.
- [13] E. Raymundo-Piñero, P. Azaïs, T. Cacciaguerra, D. Cazorla-Amorós, A. Linares-Solano, F. Béguin, *Carbon* **2005**, *43*, 786.
- [14] L.-M. A. Rodenas, D. Cazorla-Amorós, A. Linares-Solano, *Carbon* **2003**, *41*, 267.
- [15] J. Wang, S. Kaskel, *J. Mater. Chem.* **2012**, *22*, 23710.
- [16] S. Murali, J. R. Potts, S. Stoller, J. Park, M. D. Stoner, L. L. Zhang, Y. W. Zhu, R. S. Ruoff, *Carbon* **2012**, *50*, 3482.
- [17] S. H. Yoon, S. Lim, Y. Song, Y. Ota, W. M. Qiao, A. Tanaka, I. Mochida, *Carbon* **2004**, *42*, 1723.
- [18] E. Frackowiak, S. Delpeus, K. Jurewicz, K. Szostak, D. C. Amorós, F. Béguin, *Chem. Phys. Lett.* **2002**, *361*, 35.
- [19] Y. Gogotsi, P. Simon, *Science* **2012**, *335*, 167.
- [20] S. Murali, N. Quarles, L. L. Zhang, J. R. Potts, Z. Q. Tan, Y. L. Lu, Y. W. Zhu, R. S. Ruoff, *Nano Energy* **2013**, *2*, 764.
- [21] X. W. Yang, C. Cheng, Y. F. Wang, L. Qiu, D. Li, *Science* **2013**, *341*, 534.
- [22] T. Kim, S. Lim, K. Kwon, S. H. Hong, W. M. Qiao, C. K. Rhee, S. H. Yoon, I. Mochida, *Langmuir* **2006**, *22*, 9086.
- [23] J. Han, L. L. Zhang, S. Lee, J. Oh, K. S. Lee, J. R. Potts, J. Y. Ji, X. Zhao, R. S. Ruoff, S. Park, *ACS Nano* **2013**, *7*, 19.
- [24] A. Ambrosi, H. L. Poh, L. Wang, Z. Sofer, M. Pumera, *ChemSusChem* **2014**, *7*, 1102.
- [25] Y. X. Xu, C. Y. Chen, Z. P. Zhao, Z. Y. Lin, C. Lee, X. Xu, C. Wang, Y. Huang, M. I. Shakir, X. F. Duan, *Nano Lett.* **2015**, *15*, 4605.

- [26] Y. W. Zhu, S. Murali, M. D. Stoller, A. Velamakanni, R. D. Piner, R. S. Ruoff, *Carbon* **2010**, *48*, 2118.
- [27] L. B. Tang, R. B. Ji, X. K. Cao, J. Y. Lin, H. X. Jiang, X. M. Li, K. S. Teng, C. M. Luk, S. J. Zeng, J. H. Hao, S. P. Lau, *ACS Nano* **2012**, *6*, 5102.
- [28] K. S. W. Sing, *Pure Appl. Chem.* **1982**, *54*, 2201.
- [29] S. Brunauer, P. H. Emmett, E. Teller, *J. Am. Chem. Soc.* **1938**, *60*, 309.
- [30] P. I. Ravikovitch, A. V. Neimark, *Langmuir* **2006**, *22*, 11171.
- [31] D. Yang, A. Velamakanni, G. Bozoklu, S. Park, M. Stoller, R. D. Piner, S. Stankovich, I. Jung, D. A. Field, C. A. Ventrice, R. S. Ruoff, *Carbon* **2009**, *47*, 145.
- [32] M. D. Stoller, R. S. Ruoff, *Energy Environ. Sci.* **2010**, *3*, 1294.

Received: December 19, 2015
Revised: January 22, 2016
Published online: March 8, 2016